APJ, SUBMITTED
Preprint typeset using LATEX style emulateapj v. 11/10/09

arXiv:1112.0027v1 [astro-ph.CO] 30 Nov 2011

THE OPTICAL, ULTRAVIOLET, AND X-RAY STRUCTURE OF THE QUASAR HE 0435–1223[1]

JEFFREY A. BLACKBURNE[2], CHRISTOPHER S. KOCHANEK[2,3], BIN CHEN[4], XINYU DAI[4], & GEORGE CHARTAS[5]

ApJ, submitted

ABSTRACT

Microlensing has proven an effective probe of the structure of the innermost regions of quasars, and an important test of accretion disk models. We present light curves of the lensed quasar HE 0435 − 1223 in the R band and in the ultraviolet, and consider them together with X-ray light curves in two energy bands that are presented in a companion paper. Using a Bayesian Monte Carlo method, we constrain the size of the accretion disk in the rest-frame near- and far-UV, and constrain for the first time the size of the X-ray emission regions in two X-ray energy bands. The R-band scale size of the accretion disk is about $10^{15.53}$ cm ($\sim 46 r_g$), slightly smaller than previous estimates, but larger than is predicted by the standard thin disk model. In the UV, the source size is weakly constrained, with a strong prior dependence. The UV to R-band size ratio is consistent with the thin disk model prediction, with large error bars. In soft and hard X-rays, the source size is smaller than $\sim 10^{15}$ cm ($\sim 13 r_g$) at 90% confidence. We do not find evidence of structure in the X-ray emission region, as the most likely value for the ratio of the hard X-ray size to the soft X-ray size is unity. The simulations do not support the idea that quasar flux variability is due to coherent changes in accretion disk area. Finally, we find that the most likely value for the mean mass of stars in the lens galaxy is $\sim 0.3 M_\odot$, consistent with other studies.

Subject headings: accretion, accretion disks – gravitational lensing: micro – quasars: individual (HE 0435 − 1223)

1. INTRODUCTION

The structure of the innermost regions of quasars and active galactic nuclei, where the X-ray and continuum optical and ultraviolet emission originates, is not well understood. The thin accretion disk model (Shakura & Sunyaev 1973; Novikov & Thorne 1973) is widely used to explain the optical and ultraviolet (UV) continuum, but has had difficulty reproducing its observed spectral shape (e.g., Blaes et al. 2001). Some progress has been made using quasar variability (e.g., Kelly et al. 2009; MacLeod et al. 2010; Dexter & Agol 2011) and "disk reverberation" (e.g., Collier 2001), but the issue remains unclear. The structure of the X-ray emitting regions is even more mysterious, since the maximum temperature at the inner disk edge is too low to produce X-rays. Instead, a jet or a hot corona above the disk have been suggested as the X-ray source, giving rise to direct and disk-reflected spectral components (see, e.g., the review by Reynolds & Nowak 2003). Decisive tests of these models have proven elusive.

Gravitational microlensing of strongly lensed quasars has emerged as an effective technique for measuring the spatial structure of quasar accretion disks. The stars in the foreground lens galaxy magnify (or demagnify) the multiple quasar images, causing flux variability that is not correlated as would be expected from intrinsic quasar variability. The ratio of the angular size of the emission region to the Einstein radius of a star in the lens galaxy determines the strength of the variability, with large source sizes smoothing out the light curves. Since the accretion disk temperature falls with radius, the source is larger at longer wavelengths, and the microlensing effect is weaker. For a standard thin disk, where the effective temperature scales as the $\beta = 3/4$ power of the radius, the characteristic size of the disk varies with wavelength as $\lambda^{1/\beta}$. Several studies have used microlensing to put limits on accretion disk sizes, generally finding that they are larger at fixed wavelength than predicted by the thin disk model, and much larger than sizes calculated using the optical flux (Pooley et al. 2007; Anguita et al. 2008; Morgan et al. 2010). In particular, Morgan et al. (2010) find that disk sizes scale with black hole mass in a manner consistent with the $M_{\rm BH}^{2/3}$ scaling expected for a roughly constant Eddington fraction. There are also studies of the dependence of the accretion disk size on wavelength, which generally find that the size increases with wavelength (Poindexter et al. 2008; Bate et al. 2008; Eigenbrod et al. 2008; Floyd et al. 2009; Blackburne et al. 2011; Mosquera et al. 2011). One means of solving the size discrepancy is to have a flatter temperature profile, more like the $T \propto R^{1/2}$ profile of an irradiated disk (see Morgan et al. 2010), but so far the uncertainties in the slope estimates from these studies are too large to distinguish between these models. It does appear that scattering on large scales and contamination from broad line emission have too small an effect to resolve the problem (Dai et al. 2010; Morgan et al. 2010; Mosquera et al. 2011).

In general, the observed effects of microlensing are stronger in X-rays than at optical wavelengths, indicating that the X-rays are emitted from a very compact region (e.g., Pooley et al. 2007; Morgan et al. 2008; Chartas et al. 2009; Dai et al. 2010). Recently Chen et al. (2011) demonstrated that the hard X-rays from the quasar Q 2237 + 0305 are even more strongly

---

[1] Based on observations made with the NASA/ESA Hubble Space Telescope, obtained at the Space Telescope Science Institute, which is operated by the Association of Universities for Research in Astronomy, Inc., under NASA contract NAS 5-26555. These observations are associated with programs #11732 and #12324.

[2] Department of Astronomy, The Ohio State University, 140 West 18th Avenue, Columbus, OH 43210, USA; blackburne@astronomy.ohio-state.edu

[3] Center for Cosmology and AstroParticle Physics, The Ohio State University, Columbus, OH 43210, USA

[4] Homer L. Dodge Department of Physics and Astronomy, University of Oklahoma, Norman, OK 73019, USA

[5] Department of Physics and Astronomy, College of Charleston, Charleston, SC 29424, USA

microlensed than the soft X-rays, indicating that there may be temperature structure within the electron gas that presumably generates the X-ray emission.

At a redshift $z_S = 1.689$, HE 0435−1223 (Wisotzki et al. 2002; Morgan et al. 2005, hereafter HE 0435) is lensed by a foreground early-type galaxy at a redshift of $z_L = 0.46$ into four images arranged in a nearly perfect cross configuration. In this paper, we present light curves of the four images of the quasar in the *R* band and in the UV, and additionally use light curves in two X-ray energy bands from a companion paper, Chen et al. (2012, in preparation). We use these light curves to constrain the size of the source at all four wavelengths. The whole is greater than the sum of the parts: the simultaneous analysis of all four wavelengths yields better constraints than any separate "monochromatic" analysis. In addition, combining the UV emission, which is thought to originate in the inner regions of the accretion disk, with the optical emission from larger radii gives us leverage to probe the change in size of the disk with wavelength. Likewise, because we have both hard and soft X-ray light curves, we can for the first time put a quantitative constraint on the ratio of sizes in the two energy bands. Finally, we put weak constraints on the mean mass of the stars in the lensing galaxy. We outline the data in Section 2, describe our analysis method in Section 3, and discuss the results in Section 4.

2. DATA

We use eight seasons of optical *R*-band photometry resulting from an ongoing monitoring campaign using A Novel Double Imaging Camera (ANDICAM, DePoy et al. 2003) on the Small and Moderate Aperture Research Telescope System (SMARTS) 1.3-m telescope. This well-sampled light curve is supplemented by 10 epochs of UV data from the Wide Field Camera 3 (WFC3) aboard the *Hubble Space Telescope* (*HST*) and 4 epochs of X-ray data from the *Chandra X-ray Observatory*. In the rest frame of the quasar, these wavelengths correspond to the near and far UV, and to harder X-rays, but for convience we usually refer to them according to their observed-frame bands.

2.1. *Optical data*

The magnitudes of the four images of HE 0435 have been monitored since 2003 August in the *R* band (rest frame 2417 Å), with a cadence varying from one day to about a week. An automated pipeline subtracts instrumental bias and flat-fields the images in the standard way. Three to six images are obtained per epoch, and we combine them to increase the signal to noise ratio and reject cosmic rays. We measure the fluxes of the quasar images and the lens galaxy using the point spread function (PSF) fitting method described in detail by Kochanek et al. (2006). The width of the PSF is measured using the SExtractor software package (Bertin & Arnouts 1996), and we reject epochs where the full width at half maximum (FWHM) is greater than $2.''5$ or where the sky background is particularly high due to cloud cover or excessive moonlight. For the handful of remaining epochs where the magnitudes look grossly anomalous compared to neighboring epochs, we re-examine the imaging data and invariably find that an uncorrected cosmic ray has collided with one of the quasar images. We correct these cases by hand. The light curves are given in Table 1. The *R* band covers a region of the redshifted quasar spectrum free of strong emission lines, but there may be contamination from FeII emission and the Balmer continuum. However, the equivalent width is small enough that it should not strongly influence our results (see Dai et al. 2010).

We shift the light curves to correct for the light travel time delay between the quasar images. We use delay values $\Delta t_{\rm BA} = 9.5$ days, $\Delta t_{\rm BC} = 7.2$ days, and $\Delta t_{\rm BD} = -6.6$ days. These values are the result of fits to the full optical light curves using the method of Kochanek et al. (2006). Though we do not exhaustively explore the range of parameters used for these fits, the resulting values are consistent with the values of Courbin et al. (2010), and the intrinsic variability of the quasar is not strong enough for small (< 1 day) errors in the time delay corrections to have noticeable effects on our microlensing analysis. After being shifted, the light curves of images A, C, and D are resampled at the epochs of image B's light curve using linear interpolation within each individual season. We do not interpolate across seasonal gaps. Finally, we bin each season of the light curves to reduce the total number of epochs by a factor of 2. This helps to reduce the computational cost of our microlensing analysis, and does not significantly degrade our sensitivity to microlensing because its time scales are still longer than the sampling of the light curves. The delay-corrected flux ratios resulting from this processing are shown in Figure 1. Taking the ratio cancels out the intrinsic variability of the quasar, leaving only microlensing variability. At this wavelength, the microlensing variability is not dramatic, but can be seen, particularly in the $A-B$ curve between the fourth and fifth seasons.

2.2. *UV data*

HE 0435 was observed at 10 epochs between 2009 August and 2011 August using WFC3 aboard the *HST*. The observations used the F275W filter in the UVIS channel, providing flux ratios at 2750 Å (1023 Å in the source rest frame). At each epoch there are four exposures of 630 s apiece, for a total of 2520 s per epoch. For one epoch, two of the four exposures were lost to a shutter failure, but we are able to use the remaining two exposures. We use the Multidrizzle task within the PyRAF software package[6] to combine the four flatfielded images and reject cosmic rays. The world coordinate systems (WCSs) provided with the images enables the software to accurately align the images. Examining the bad pixel masks produced by this process, we find that several pixels at the center of each quasar image are incorrectly marked as cosmic rays, so we manually edit the masks to mark these pixels as good, and repeat the final drizzle step. The result is a single clean and accurate image for each epoch. At this wavelength, the images are remarkably empty, with few sources approaching the brightness of the lensed quasar. In particular, the lens galaxy and quasar host galaxy are not detected.

We use DoPHOT (Schechter et al. 1993) to perform aperture photometry on the quasar components in each epoch, using an aperture $0.''85$ on a side, wide enough to capture essentially all of the flux in a given quasar component but small enough that the other components do not contaminate the photometry. We convert the instrumental fluxes into ST magnitudes using the standard header keywords PHOTFLAM and PHOTZPT. In this filter, the offset from ST to AB magnitudes is $m_{\rm AB} - m_{\rm ST} = 1.532$. The ST magnitudes of the four quasar components for all 10 epochs are listed with their formal uncertainties in Table 2, and the magnitude differences are plotted in Figure 1. The magnitudes in Table 2 are uncorrected for

---

[6] PyRAF and Multidrizzle are products of the Space Telescope Science Institute, which is operated by AURA for NASA.

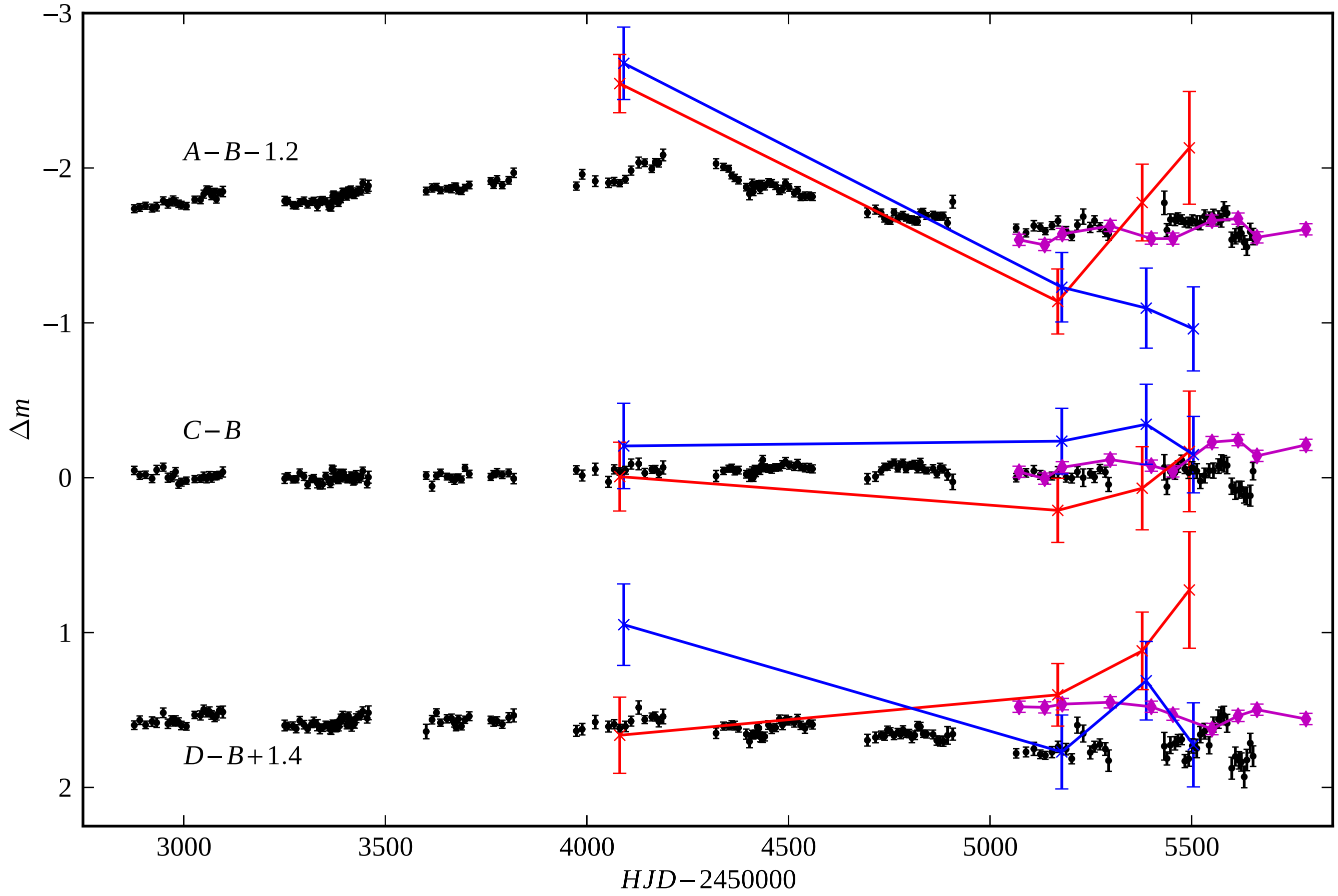

FIG. 1.— Light curves of the flux ratios between the images of HE 0435, expressed in magnitudes. Black circles, magenta diamonds, red crosses, and blue crosses show the *R*-band, UV, soft X-ray, and hard X-ray data, respectively. The curves have been corrected for the lensing time delays as described in the text, and the optical light curve has been binned by a factor of two. Any remaining variability is considered to be due to microlensing. The light curves as shown are the input to the microlensing simulation. It is clear that the X-ray light curves have significantly more microlensing variability than the optical and UV curves.

Galactic extinction, which we calculate to be 0.36 magnitudes along this sightline, using the Schlegel et al. (1998) value and the Cardelli et al. (1989) $R_V = 3.1$ extinction law. Since we are only concerned with magnitude differences, this overall offset has no effect on our calculations. At the redshift of this quasar, Lyβ OVI, and other emission lines overlap with the F275W filter, but the passband is wide enough that the continuum dominates the flux; we estimate that about 10% of the total flux is in the emission lines. Contamination from the spatially extended emission line region may bias our results toward larger UV source sizes, but the effect should not be a strong one (Dai et al. 2010). Because the latest epoch of UV data extends beyond our optical light curve, and because our simulations were begun before it was collected, we use only the first 9 epochs of the UV light curves for our microlensing simulations.

We shift the UV light curves of quasar images A, C, and D according to the time delays given in Section 2.1, and use linear interpolation to resample them contemporaneously with B. The time delays between the quasar images are small compared to the typical separation between epochs, so the adjustments are small. But there is potential for systematic error because of intrinsic quasar variability that is not well-described by our linear interpolation, so we broaden the uncertainties on the light curves to account for this. To estimate this extra uncertainty, we scale and shift the *optical* light curves so that they match as closely as possible the UV light curves, and treat them as an estimate of the UV variability. The typical absolute difference between the interpolated UV magnitudes and the scaled and shifted optical light curve is ∼0.036 mags, and we add this in quadrature to the formal uncertainties. Since the statistical uncertainties are so small, this systematic contribution dominates the error budget for the UV light curves.

The lack of flux from the lens galaxy in the UV affords us an opportunity to investigate the existence of a fifth image of the quasar. Lensing theory generically predicts an odd number of quasar images, but in practice lensed quasars almost always have either 2 or 4 observed images. The "missing image" is located at the maximum of the light travel time near the center of the lens galaxy, and is strongly demagnified due to the sharp curvature of the potential (Rusin & Ma 2001; Mao et al. 2001; Keeton 2003; Rusin et al. 2005). This makes central images an interesting probe of both the innermost density profiles and central black holes of distant galaxies, but so far only two central images have been unambiguously detected (Winn et al. 2004; Inada et al. 2005, 2008). To check for a central image at UV wavelengths, we create a deep image of HE 0435 by stacking the frames from every epoch using Multidrizzle. There are small (∼1″) offsets between the WCSs of each epoch, so we measure the pixel shifts between the single-epoch images using cross-correlation and provide them

TABLE 1
R-BAND LIGHT CURVES

HJD − 2450000	A	B	C	D
2863.883	2.065 ± 0.012	2.632 ± 0.019	2.592 ± 0.018	2.821 ± 0.022
2871.829	2.140 ± 0.014	2.628 ± 0.022	2.561 ± 0.019	2.790 ± 0.023
2877.843	2.134 ± 0.012	2.644 ± 0.017	2.670 ± 0.016	2.803 ± 0.018
2884.784	2.141 ± 0.012	2.653 ± 0.017	2.661 ± 0.017	2.870 ± 0.019
2891.827	2.172 ± 0.015	2.689 ± 0.023	2.685 ± 0.022	2.831 ± 0.024
2899.843	2.171 ± 0.012	2.728 ± 0.018	2.712 ± 0.017	2.856 ± 0.019
2906.848	2.184 ± 0.008	2.729 ± 0.011	2.745 ± 0.011	2.891 ± 0.012
2916.803	2.192 ± 0.010	2.720 ± 0.015	2.713 ± 0.014	2.953 ± 0.016
2919.828	2.177 ± 0.013	2.759 ± 0.020	2.738 ± 0.019	2.910 ± 0.021
2926.780	2.186 ± 0.012	2.736 ± 0.018	2.643 ± 0.016	2.885 ± 0.019

NOTE. — Light curves are in uncalibrated magnitudes. This table is published in its entirety online. A portion is shown here for guidance regarding its form and content.

TABLE 2
ULTRAVIOLET LIGHT CURVES

HJD − 2450000	A	B	C	D
5072.079	18.566 ± 0.002	18.917 ± 0.003	18.867 ± 0.003	19.005 ± 0.003
5135.646	18.664 ± 0.003	19.004 ± 0.003	18.983 ± 0.003	19.096 ± 0.003
5179.185	18.830 ± 0.004	19.198 ± 0.005	19.146 ± 0.005	19.288 ± 0.006
5298.162	18.780 ± 0.003	19.197 ± 0.003	19.090 ± 0.003	19.247 ± 0.004
5400.013	18.684 ± 0.003	19.064 ± 0.003	18.953 ± 0.003	19.136 ± 0.003
5453.678	18.889 ± 0.003	19.244 ± 0.004	19.204 ± 0.003	19.408 ± 0.004
5550.662	18.992 ± 0.003	19.433 ± 0.004	19.219 ± 0.003	19.676 ± 0.004
5615.296	18.878 ± 0.003	19.323 ± 0.004	19.104 ± 0.003	19.443 ± 0.004
5662.224	18.742 ± 0.003	19.066 ± 0.003	18.949 ± 0.003	19.119 ± 0.003
5783.750	18.450 ± 0.003	18.854 ± 0.003	18.642 ± 0.003	19.012 ± 0.004

NOTE. — Light curves are in ST magnitudes.

to Multidrizzle. We use PSF fitting to carefully subtract the wings of the four bright quasar images and test for a central image. The PSF model is constructed from the (exposure-weighted) sum of oversampled and appropriately rotated Tiny Tim PSFs for the set of 10 epochs. We fix the relative positions of the five quasar images, using the positions of the bright four and of the lens galaxy from the CASTLES database (Falco et al. 2001), and allow the overall position offset and the five normalizations to vary. We rule out a central image brighter than 26.3 ST magnitudes at 95% confidence; this implies a flux ratio relative to the faintest image $f_5/f_D < 0.002$. This non-detection probably arises from either a massive central black hole or a steep density profile in the lens galaxy, but it is difficult to say anything more quantitative from these UV observations because of the possibility of extinction within the lens galaxy. Likewise, if we *had* detected flux in the central regions, distinguishing quasar emission from nuclear star formation or weak AGN activity in the lens galaxy would have been difficult with these observations.

2.3. *X-ray data*

HE 0435 was observed on 2009/12/07, 2010/07/04, and 2010/10/29 using *Chandra*/ACIS (Weisskopf et al. 2002; Garmire et al. 2003), with an exposure time of 12.8 ks for each observation. Including an archival observation made in 2006 (Blackburne et al. 2011; Pooley et al. 2011), we have accumulated four *Chandra* observations of the quasar. The details of the reduction of these observation are presented in a companion paper (Chen et al. 2012, in preparation). We separate the photon events into soft (0.4 – 1.3 keV) and hard (1.3 – 8.0 keV) energy bands and perform imaging and spectral analyses of the four images of HE 0435 in these bands and in the full energy range. In the spectral analysis, we fit the spectra using a power law plus Gaussian emission line model, representing the X-ray continuum and the Fe Kα emission line, both modified by Galactic absorption and absorption at the lens redshift. In the imaging analysis, we use PSF fitting to determine the photon flux for each image in each epoch and each band. After obtaining the best fits from the imaging analysis, we correct for absorption to obtain the intrinsic photon fluxes for each image. The resulting four-epoch X-ray light curves for each quasar image in three energy bands are presented by Chen et al. (2012), and we use the soft and hard band light curves in our simulations. The flux ratios, expressed as magnitude differences, are shown in Figure 1.

Since the X-ray light curves are even more sparsely sampled than the UV light curves, it seems inappropriate to use interpolation to attempt a correction for the systematic errors caused by lensing time delays combined with intrinsic quasar variability. Instead, we simply leave the X-ray fluxes uncorrected, and broaden the uncertainties to account for this error source. Unlike the UV light curves, the statistical uncertainties are much larger than the systematic errors that we expect from time delays.

3. METHOD

To constrain the source properties (i.e., the size and shape of the quasar emission regions) and lens properties (i.e., the mean mass of stars and peculiar velocity), we use many simulated light curves. These simulations are compared to the observed light curves and evaluated using a chi-square estimator. Each simulated light curve, which is associated with a particular vector in parameter space, is thus assigned a likelihood. We add them together to create a joint likelihood distribution, which we then combine with priors on the parameters to generate posterior probability distributions for the quantities of interest using Bayes' theorem. This Bayesian Monte Carlo approach is laid out in detail by Kochanek (2004), and we use a version that is updated by Poindexter & Kochanek (2010b) to include the random motions of the microlens stars.

We model the light curves for the four quasar components at each of the four wavelengths as an independent intrinsic quasar light curve S modified by a time-invariant and achromatic macro-magnification μ_i due to the overall gravitational potential of the lens galaxy, by the magnification due to microlensing $\delta\mu_i$, and by a time-invariant "catch-all" term $\Delta\mu_i$. This last term represents several possible systematic effects, such as differential extinction in the lens galaxy (e.g., Falco et al. 1999; Mosquera et al. 2011), millilensing by dark matter substructure (e.g., Kochanek & Dalal 2004; Fadely & Keeton 2011), systematic errors in the macro-magnification μ_i, or low levels of unrecognized contamination of the quasar flux by the lens or host galaxy. Expressing these quantities in magnitudes, this is

$$\begin{aligned} m_i\left(t_j,\lambda_k\right) &= S\left(t_j,\lambda_k\right)+\mu_i+\Delta\mu_i(\lambda_k)+\delta\mu_i\left(t_j,A(\lambda_k)\right) \\ &= S\left(t_j,\lambda_k\right)+\mu_{i,\mathrm{tot}}\ , \end{aligned} \qquad (1)$$

where i enumerates the four quasar components (A, B, C, and D), and t_j and λ_k denote the set of epochs and wavelength in our light curves. The function $A(\lambda_k)$ is the area of the quasar emission profile at wavelength λ_k; it is through this function that the microlensing term $\delta\mu_i$ depends on wavelength.

3.1. *Microlensing Simulations*

We simulate the microlensing parts of our model (i.e., the $\delta\mu_i$ term) using microlensing magnification patterns created using the particle-particle/particle-mesh (P3M, Hockney & Eastwood 1981) method detailed by Kochanek (2004). The patterns give the microlensing magnification of each quasar image as a function of the source's position. The patterns appear as a network of intertwined high-magnification caustics separated by lagoons of lower magnification. Like Poindexter & Kochanek (2010a,b), we use dynamic patterns, meaning that they are recalculated for each epoch. This allows us to take into account the random velocities of the stellar microlenses as well as the parallactic motion of the earth. The patterns are periodic by construction in both the lens and source planes, allowing us to wrap light curves and stellar motions across the edges, and eliminating edge effects when convolving the patterns.

The general characteristics of the magnification patterns are determined by the shear γ and the convergence $\kappa_{\mathrm{tot}} = \kappa_s + \kappa_*$, where κ_s is the convergence due to smoothly distributed matter and κ_* is due to the microlens stars. These quantities, as well as the macro-magnifications μ_i, are determined by modeling the lensing of the system as a whole. We use the extensive models of Kochanek et al. (2006), who parameterize the relative contributions of stars and of the dark matter halo using $f_{M/L}$, the normalization of the stellar component relative to its best-fit normalization with no dark matter halo. The particular models we use set the effective radius of the stellar component R_e to $0\farcs86$ and the break radius of the Navarro-Frenk-White (NFW) halo r_c to $10\farcs0$. We use three values of $f_{M/L}$: 0.1, 0.3, and 1.0. This allows us to explore a range of values for this parameter, and for all of our results we marginalize over it. Although there are reasons to prefer a low value of $f_{M/L}$ (see, e.g., Kochanek et al. 2006), we conservatively elect not to apply a prior on its value. This choice has almost no effect on our results.

We randomly scatter stars across the region near each quasar component to create the microlens convergence κ_*. Their masses are drawn from a power-law mass function with $dN/dM \propto M^{-1.3}$, with a dynamic range of 50 between its maximum and minimum masses. This a reasonable match to stellar mass functions (Poindexter & Kochanek 2010b), and the details should have little effect on our results (e.g., Wyithe et al. 2000). We use a range of values for the mean mass of the stars, with $\langle M/M_\odot\rangle = 0.03$, 0.1, 0.3, 1, 3, and 10. The magnification patterns' outer dimensions are 20 times the Einstein radius R_{Ein} of this mean mass, where

$$\begin{aligned} R_{\mathrm{Ein}} = D_{\mathrm{OS}}\theta_{\mathrm{Ein}} &= \left(\frac{4G\langle M\rangle}{c^2}\frac{D_{\mathrm{OS}}D_{\mathrm{LS}}}{D_{\mathrm{OL}}}\right)^{1/2} \\ &= (5.42\times10^{16}\ \mathrm{cm})\langle M/M_\odot\rangle^{1/2}\ , \end{aligned} \qquad (2)$$

and $(D_{\mathrm{OL}}, D_{\mathrm{OS}}, D_{\mathrm{LS}}) = (1203, 1746, 1093)$ Mpc are the angular diameter distances from observer to lens, observer to source, and lens to source, respectively, for $\Omega_M = 0.3$, $\Omega_\Lambda = 0.7$, and $H_0 = 70\,\mathrm{km\,s^{-1}\,Mpc^{-1}}$. The patterns used for the optical wavelength simulations are 4096 pixels on a side, so that their pixel size is approximately $2.6\times10^{14}\langle M/M_\odot\rangle^{1/2}$ cm. Since the mass of the central black hole is $\sim 5\times10^8 M_\odot$ (based on the C IV line width, Peng et al. 2006), this pixel size is about $3.6\langle M/M_\odot\rangle^{1/2}$ gravitational radii. Since the emission is more compact at UV and X-ray wavelengths, for these simulations we create more detailed versions of the same patterns, doubling the resolution to 8192 pixels. Care must be taken when recreating the patterns at higher resolution, because of certain details of the pattern creation algorithm. Specifically, the shear γ is adjusted slightly from the input value so that the periodic scale is an integer number of pixels in both planes. When creating the high-resolution patterns we intentionally calculate this adjustment as if the pattern dimension were 4096 instead of 8192. This results in the desired periodicity, and avoids small distortions of the new pattern relative to the old.

For each quasar image, the microlensing variability is simulated by the movement of the quasar across the pattern, as well as the evolution of the pattern itself due to the random motions of the stars. The latter is made possible by our dynamic patterns, where each star's position is dependent on epoch. We use a one-dimensional velocity dispersion of $255\,\mathrm{km\,s^{-1}}$ in the lens rest frame, estimated from the Einstein radius of a singular isothermal sphere (SIS) model of the lens. Treu et al. (2006) have shown this to be a good estimator for the stellar velocity dispersion. We assume that the lens galaxy has negligible bulk rotational velocity. The effective velocity of the source across the pattern is the vector sum of the peculiar velocities of the observer, the lens, and the source, properly scaled for geometry and cosmological time dilation. We follow the approach of Poindexter & Kochanek (2010b), taking for the observer's motion the cosmic microwave background (CMB) dipole velocity (from Hinshaw et al. 2009) projected perpendicular to the line of sight, combined with the parallax due to the earth's orbit, and treating the remaining two velocities as normally distributed random variables. For HE 0435, the projected CMB velocity is $(363, -56)\,\mathrm{km\,s^{-1}}$ East and North, respectively. Using the empirical interpolation of Mosquera & Kochanek (2011), we estimate that the rest-frame peculiar velocity dispersions for the lens and the source are $\sigma_L = 277$ and $\sigma_S = 227\,\mathrm{km\,s^{-1}}$, respectively. Cosmological time dilation and geometric projection effects combine to suppress the contribution of the source, so that the lens velocity dominates the effective velocity of the source across the pattern. The dispersion of the prior on the effective velocity, projected to the lens plane, is given by[7]

$$\sigma_{\rm eff}^2 = \sigma_L^2 + \sigma_S^2 \left(\frac{1+z_L}{1+z_S}\right)^2 \left(\frac{D_{\rm OL}}{D_{\rm OS}}\right)^2 = \left(290\,{\rm km\,s^{-1}}\right)^2 \ . \quad (3)$$

The finite size of the source is simulated by convolving the magnification patterns with the source's emission profile. We use a standard thin disk model that radiates as a multi-temperature blackbody, with an effective temperature that varies inversely with the $\beta = 3/4$ power of the radius. We neglect the inner edge of the disk. Although it is not guaranteed that this is the correct model for the accretion disk, in practice the details of the source's radial profile are not very important (Mortonson et al. 2005; Congdon et al. 2007). The wavelength-dependent area of the disk $A(\lambda)$ is defined as the area within the contour where $k_B T_{\rm eff} = hc/\lambda$. We vary this area in logarithmic intervals of 0.2 dex, using an adaptive algorithm to explore the peak of the likelihood function, and stopping when the source is too small to be resolved by the magnification pattern pixels, when the likelihood falls to a very small fraction of the peak value, or when 30 values of the area have been explored. Like Poindexter & Kochanek (2010a), we also vary the inclination of the disk $\cos i$ and the position angle of its major axis ϕ_a. We use ten inclinations, with $\cos i$ ranging from 1.0 (face-on) to 0.1 (nearly edge-on) in steps of 0.1. Similarly, we use 18 major axis position angles, ranging from 0° to 170°. The inclination and major axis position angle do not vary with wavelength, but the area is allowed to vary independently in our four bands.

3.2. *Bayesian Monte Carlo*

A handful of parameters determine the exact shape of the microlensing light curve: the source parameters (A, $\cos i$, and ϕ_a), the lens parameters ($\langle M \rangle$ and $f_{M/L}$), and a particular starting point and effective velocity of the path across the magnification pattern. As described in detail by Kochanek (2004) and Poindexter & Kochanek (2010b), we use Monte Carlo integration to evaluate the Bayesian integrals over the space of these parameters. For each combination of source and lens parameters, we evaluate 10^5 trial paths across the magnification patterns. Each trial is evaluated using the chi-square statistic

$$\chi_k^2 = \sum_i \sum_j \left[\frac{m_i\left(t_j,\lambda_k\right) - S\left(t_j,\lambda_k\right) - \mu_{i,\rm tot}}{\sigma_i\left(t_j,\lambda_k\right)}\right]^2 \ , \quad (4)$$

where σ_i are the measurement uncertainties. The intrinsic quasar light curve $S\left(t_j,\lambda_k\right)$ and the "catch-all" term $\Delta\mu_i(\lambda_k)$ are determined for each trial by minimization of χ_k^2. Trials with chi-square values above a predefined cutoff value are discarded, as their contribution to the likelihood is negligible. We do not impose any prior on the intrinsic light curve, though in principle one could grant a greater weight to trials that yield light curves with statistical properties matching those of other quasars of similar luminosity and redshift (see, e.g., Kozłowski et al. 2010; MacLeod et al. 2010). We do impose a Gaussian prior on $\Delta\mu_i$, with a mean of 0 mags and a variance of $(0.1\,{\rm mag})^2$. It is worth asking whether it is appropriate to allow these quantities to vary independently at various wavelengths, as we have done. It is reasonable to expect correlations between wavelengths in the quasar light curve, so if we impose a prior on the light curve in future work, it ought to include such correlations. Forgoing a prior broadens our error bars, and is thus the conservative choice. We make a similar conservative choice in allowing $\Delta\mu_i$ to vary with wavelength, since some of its contributors are wavelength-dependent (e.g., flux contamination from the lens galaxy at optical wavelengths, or differential extinction/absorption by the interstellar medium of the lens).

We are interested in trials that provide simultaneous good fits to our optical, UV, and X-ray light curves. In principle, it is possible to simultaneously evaluate χ^2 for a given trial at all wavelengths, but given the length of our light curves, particularly in the optical, we find it less computationally demanding to treat the four wavelengths separately. We first amass a collection of trials that provide reasonable fits to our R-band data, and then resimulate each of these using an independently varied source area for the UV light curve. This results in a new set of trials that fit both the optical and UV data. There is a balance between adding and removing trials, since each input trial generates a number of new trials with a range of UV source areas, but some of these are rejected due to the χ^2 cutoff. Each of the resulting trials has the same parameters as the trial from which it was generated, and additionally a value for the UV source area and a UV chi-square value and $N_{\rm dof}$. We continue this process for the soft and hard X-ray light curves, using the output of one simulation as the input for the next, and obtaining in the end a final set of trials with independent optical, UV, and soft and hard X-ray source areas.

We convert chi-square values to likelihoods using an incomplete Gamma function, as derived by Kochanek (2004). This function is robust to small errors in the light curve uncertainties, even with many degrees of freedom; in essence, it does not give "extra credit" to solutions with $\chi^2/N_{\rm dof} < 1$. We adapt it for multiwavelength use, defining the likelihood as

$$\mathcal{L} \propto \Gamma\left(\sum_k \frac{N_{{\rm dof},k}}{2} - 1, \sum_k \frac{\chi_k^2}{2f_{0,k}^2}\right) \ , \quad (5)$$

where χ_k^2 and $N_{{\rm dof},k}$ are the chi-square and degrees of freedom at wavelength λ_k, and $f_{0,k}^2$ is the factor by which we rescale the chi-square to account for errors in the uncertainties. For the optical, UV, soft X-ray, and hard X-ray light curves, respectively, $N_{{\rm dof},k}$ is 585, 24, 9, and 9, $f_{0,k}^2$ is 2.0, 1.75, 1.25 and 1.25, and the cutoff values of χ_k^2, above which trials are discarded, are 4.0, 3.5, 2.5, and 2.5. We multiply the resulting likelihood distribution by appropriate priors to generate posterior probability distributions for the parameters of interest, marginalizing over the less-interesting parameters. The prior is uniform for the starting position of the trial paths, and normally distributed as described in Section 3.1 for their effective velocities. For the other parameters, we use uniform logarithmic or linear priors. In particular, for the area of the source we explore the results of using both priors.

4. RESULTS AND DISCUSSION

Figures 2 and 3 show posterior probability distributions for the projected area of the quasar. In Figure 2 we plot the joint

---

[7] In their Equation 12, Poindexter & Kochanek (2010b) neglect a factor of $(1+z_S)$ in the scaling of σ_S, but this introduces only a negligible error in their velocity prior.

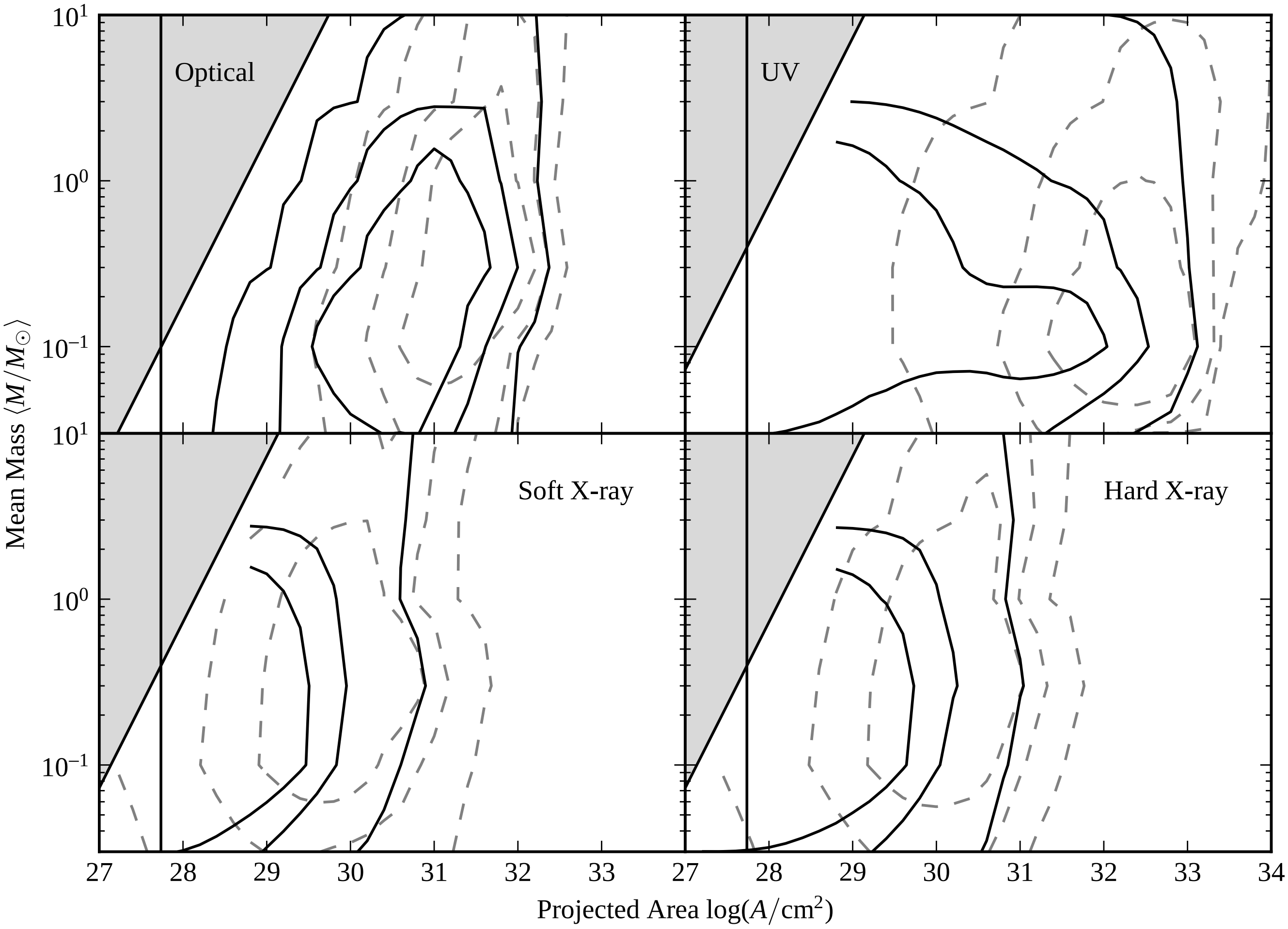

FIG. 2.— Joint posterior probability distributions for the projected area of the source and the microlens mean mass. The contours show 39%, 86%, and 99% enclosed probability (note the non-standard values). Black curves denote the logarithmic prior, and gray dashed curves the linear prior. The shaded zone indicates the region where the source area is smaller than the pixel size of the magnification patterns. The square of the black hole's gravitational radius (for $M_{\rm BH} = 5 \times 10^8 M_\odot$) is shown with a vertical line. All other parameters are marginalized.

distribution of the source area and the mean microlens mass at optical and UV wavelengths and in both soft and hard X-ray energy bands, which are the result of the combined analysis of the light curves at all wavelengths. All other parameters have been marginalized. The black contours show the results for a logarithmic prior on the source area, and the gray contours are for a linear prior. Ideally, we would like to have results that are independent of the priors, but single-epoch and sparsely-sampled microlensing results tend to have some prior dependence. In general, a logarithmic prior is appropriate for a positive scale-free parameter like the source size (or area), since it makes no sense to give, e.g., the range 1 – 10 cm ten times the weight of 0.1 – 1 cm. However, on small scales between the innermost stable orbit and the size associated with the sampling of the light curve, a linear prior is arguably more appropriate. One possible approach would be to use a "hybrid" prior such as $A/(A + r_g^2)$ that acts linearly at source areas that are small relative to the square of the black hole's gravitational radius and more like a logarithmic prior for larger areas. For ease of comparison with other results, however, we stay with the traditional uniform priors. With a logarithmic prior we cannot put a lower limit on the UV or X-ray size, but the distribution increases with decreasing area until it hits the resolution limit of our magnification patterns, depicted as a shaded region in Figure 2. In the top panels of Figure 3 we plot the projection of this joint distribution along the vertical axis, marginalizing over $\langle M \rangle$. The effect of the resolution limit can be seen on the logarithmic prior (black) curves, causing an artificial decrease in probability at small source areas. In the bottom panels of Figure 3 we avoid this problem by taking a slice across the joint distribution at fixed $\langle M \rangle = 0.3 M_\odot$. With a logarithmic prior, we find that in the R band $\log(A/\mathrm{cm}^2) = 30.87^{+0.63}_{-0.66}$ (68% confidence), while in the soft and hard X-ray bands, respectively, $\log(A/\mathrm{cm}^2) < 29.63$ and 29.85 at 90% confidence. Because our resolution limit prevents the X-ray distributions from converging, the confidence level is probably higher than 90%. The UV area has a very broad distribution which decreases more or less monotonically from the resolution limit out to larger areas, with a tail extending to larger areas than even the optical distribution. Since the linear prior puts a much greater weight on larger sources, these distributions are biased high relative to the logarithmic prior, especially in the UV, where the area distribution is wide. With this prior, the logarithm of the source areas in the R band, the soft X-ray band, and the hard X-ray band are $31.57^{+0.39}_{-0.51}$, $29.93^{+0.63}_{-0.75}$, and $30.16^{+0.56}_{-0.73}$, respectively. Since the UV distributions are so broad and so prior-dependent, it is probably best to view the UV result as inconclusive. In Figures 2

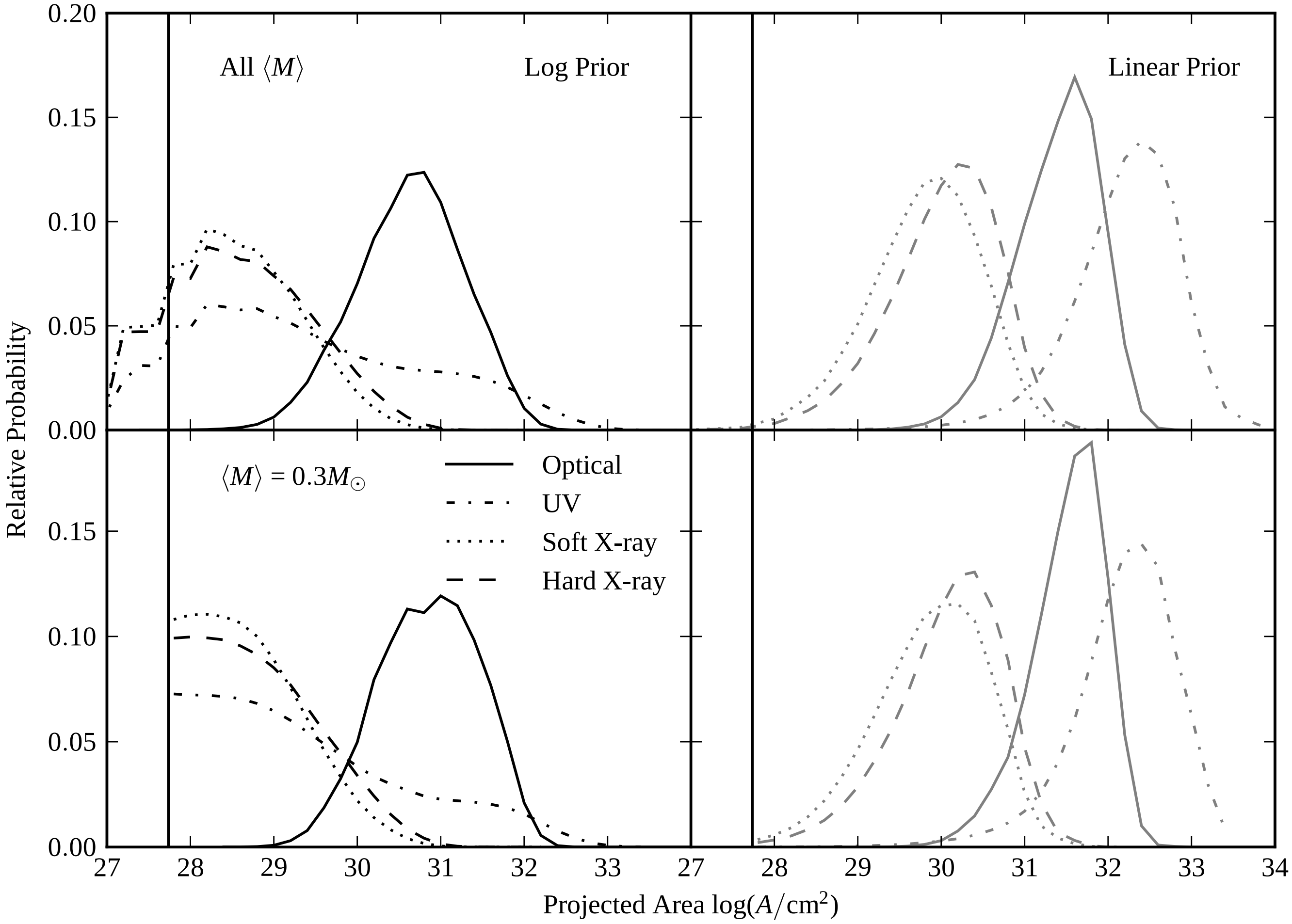

FIG. 3.— Posterior probability distributions for the projected area of the region producing the observed-frame *R* band, UV, soft X-ray, and hard X-ray emission. The left (right) two panels use a logarithmic (linear) prior. In the top panels, all other variables have been marginalized, including $\langle M \rangle$, leading to an artificial decrease in probability at small areas (see Figure 2). In the bottom panels, $\langle M \rangle$ is fixed at $0.3M_\odot$. In all panels, the square of the black hole's gravitational radius is marked with a vertical line.

and 3 we plot the square of the black hole's gravitational radius as a vertical line, using the Peng et al. (2006) mass of $5 \times 10^8 M_\odot$. We can think of this as a hard lower limit on the area, keeping in mind that the black hole mass is uncertain by a factor of 3 or so. Aside from this we cannot set a lower limit on the UV or X-ray size without resorting to the linear prior.

It is interesting to ask which combinations of wavelengths have the greatest power to constrain the area. Obviously, without the UV light curves we have no information about the corresponding source size, and likewise in X-rays. Nor have we simulated either the hard or soft X-ray or UV in the absence of the *R*-band light curve. But what improvement on the optical size is achievable by adding, e.g., just the UV data? Figure 4 shows the source area probability distributions obtained from each step in our sequence of simulations. The top panels show the constraint on the *R*-band area resulting from modeling only the optical light curve. With a logarithmic prior, it is broad enough that it does not converge at small areas. Adding additional constraints from the UV (middle panels) and soft X-ray (bottom panels) light curves cause the optical size distribution to become narrower, particularly in the X-ray case. Comparing this figure to the lower panels of Figure 3, it is clear that the addition of the X-ray data has significant power to exclude small-area solutions for the optical size. This is to be expected given the greater variability seen in the X-ray band than at other wavelengths (see Figure 1). The high X-ray variability rules out low-velocity solutions which are the only way that a very small optical source can exhibit (relatively) small amplitudes of variability. The X-ray and UV data have relatively modest effects on each other's distributions.

The inclination of the accretion disk and the position angle of its major axis have subtle effects on the microlensing light curves, and can only be realistically simulated with dynamic magnification patterns, as is done for Q 2237+0305 by Poindexter & Kochanek (2010a). The microlensing variability of HE 0435 is not as prominent as that of Q 2237, and its lensing geometry is such that the random stellar motions are less important relative to the motion of the source across the patterns. For these reasons, it is not surprising that our posterior probability distributions show no significant preference for particular values of the inclination $\cos i$ and the major axis position angle ϕ_a. Therefore, we treat these parameters as undetermined, and simply marginalize the likelihood over them.

Since A is its *projected* area of the accretion disk, it depends both on the physical size of the disk and its inclination, in the sense that more highly inclined disks must be larger to present the same area. When calculating the Bayesian integrals, we construct posterior probability functions for the disk's scale

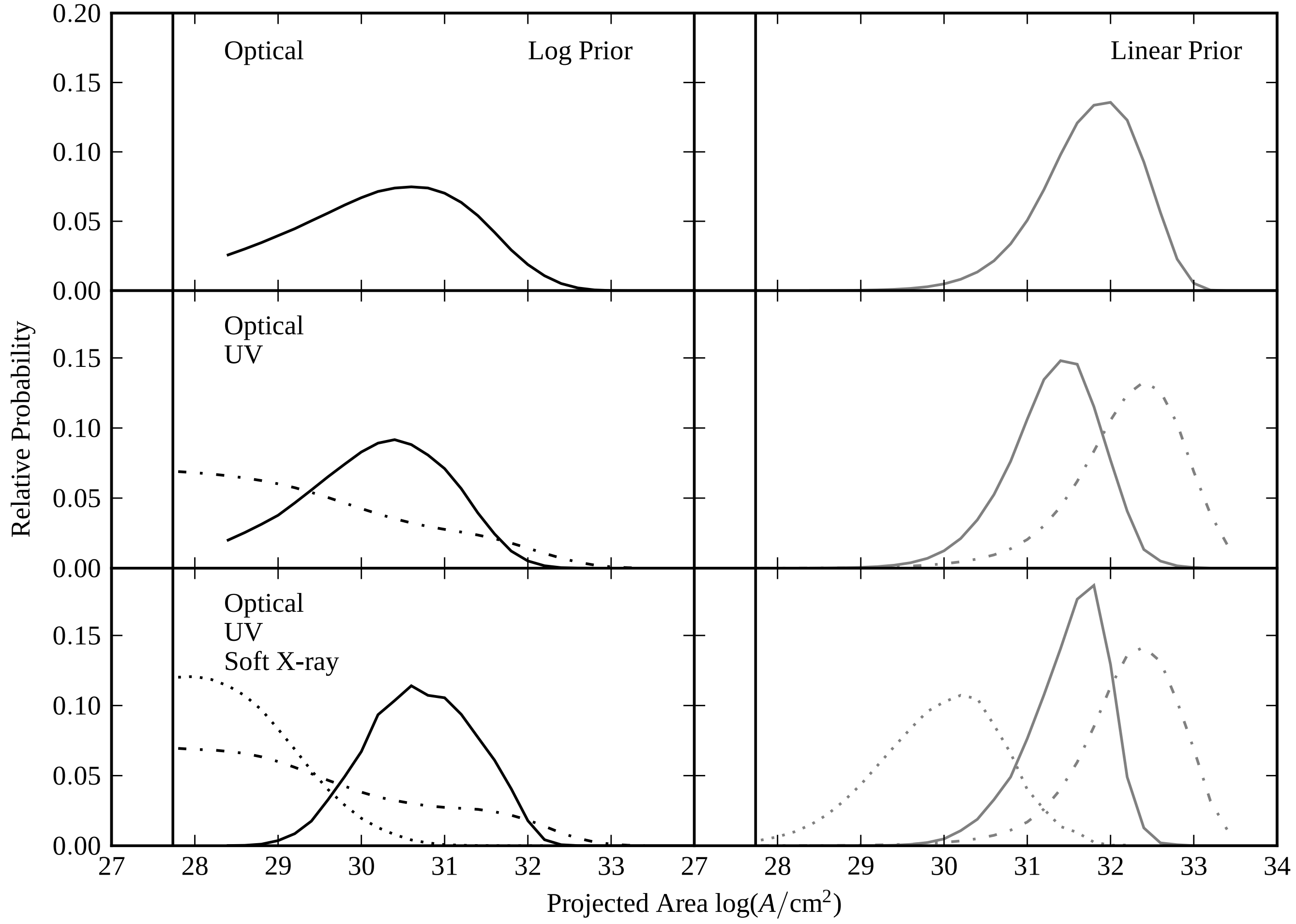

FIG. 4.— Posterior probability distributions for the projected area of the source for fixed $\langle M\rangle = 0.3M_{\odot}$,constrained by various combinations of data. Top panels: optical source area, constrained only by the *R*-band light curve. Middle panels: optical (solid) and UV (dot-dashed) source areas, constrained by *R*-band and UV light curves. Bottom panels: optical, UV, and soft X-ray (dotted) source areas, constrained by the *R*-band, UV, and soft X-ray light curves. The left (right) panels use a logarithmic (linear) prior. The square of the black hole's gravitational radius is shown with a vertical line. Compare to the bottom panels of Figure 3, where the source areas are constrained by all four light curves.

radius $R_S(\lambda)$, removing the inclination effects. This parameter is the radius in the thin disk where $k_B T_{\mathrm{eff}}(r) = hc/\lambda$. Assuming the accretion disk temperature slope $\beta = 3/4$ as in the thin disk model, it is related to the half-light radius of the accretion disk by the factor $R_{1/2}/R_S = 2.44$. The posterior probability distributions for R_S are shown in Figure 5 for fixed $\langle M\rangle = 0.3M_{\odot}$. With a logrithmic prior on the scale radii, we find an *R*-band size $\log(R_S/\mathrm{cm}) = 15.53^{+0.36}_{-0.35}$. By way of comparison, for the adopted black hole mass of $5\times10^8 M_{\odot}$, an Eddington ratio of 0.3, and an accretion efficiency of 0.1, at this wavelength thin disk theory predicts a value of 15.12. A flux-based estimate yields a value of 14.74, assuming $\beta = 3/4$. (See, e.g., Mosquera & Kochanek (2011) for a description of these two estimators.) In the UV we can place a 90% confidence upper limit on the size $\log(R_S/\mathrm{cm}) < 15.77$, consistent with both the theory size of 14.63 and the flux size of 14.24. The expected theory sizes for the optical and UV disk are shown in Figure 5. The soft and hard X-ray radii have probability distributions similar to each other, indicating sizes smaller than 14.96 and 15.07 at 90% confidence, respectively. With the logarithmic prior, the UV and X-ray distributions all show a small decline at the smallest radii, but this is a resolution artifact similar to the one shown in Figure 3. Namely, at the smallest scale radii only face-on disks are resolved, so only trials with $\cos i \approx 1$ contribute. This artifact is only important for the two leftmost data points in Figure 5. Our logarithmic-prior estimate for the *R* band disk half-light radius, $\log(R_{1/2}/\mathrm{cm}) = \log(2.44R_S/\mathrm{cm}) = 15.92^{+0.36}_{-0.35}$, is slightly smaller than, but still consistent with previous estimates at similar wavelengths. Morgan et al. (2010), Blackburne et al. (2011) and Mosquera et al. (2011) respectively find values of $16.1^{+0.5}_{-0.7}$, 16.04 ± 0.38, and $16.32^{+0.27}_{-0.84}$. In comparing these results, we note that our present calculations account for more sources of systematic uncertainty than these other studies, which is why they have comparable uncertinties despite using superior data.

Our model parameterizes the dependence of the disk area on wavelength using the area at each wavelength, rather than a normalizing area and power-law slope. Since the X-rays do not originate from thermal thin disk emission, only the optical and UV sizes constrain the wavelength slope. Therefore the two approaches are equivalent in our case, with two parameters each. To estimate the dependence of disk area on wavelength, we calculate posterior probability distributions for the ratio of areas. Figure 6 shows distributions for the logarithm of the UV area to optical area ratio, along with similar dis-

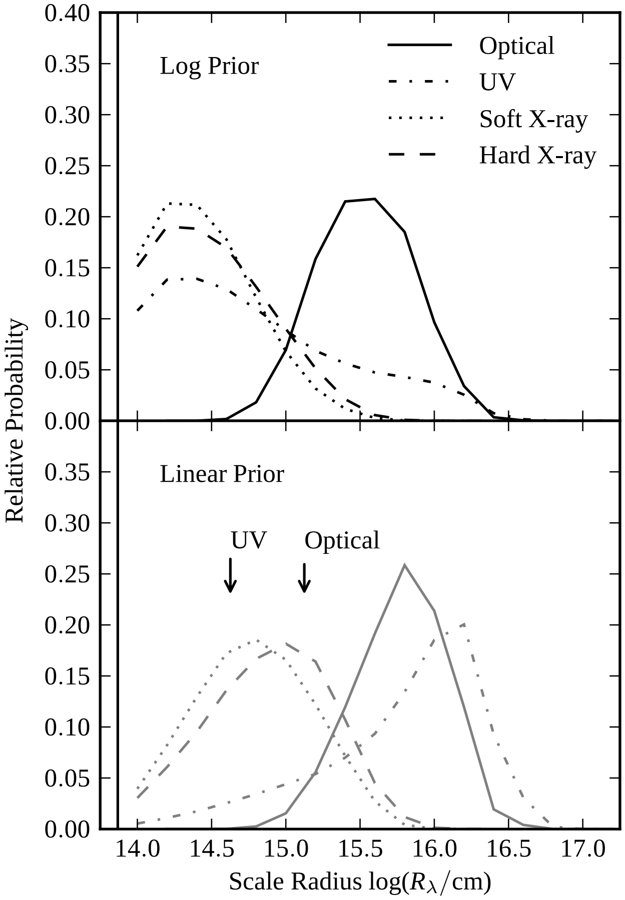

FIG. 5.— Posterior probability distributions for the scale radius of the source at a variety of wavelengths. The top (bottom) panel uses a logarithmic (linear) prior. The arrows mark the observed-frame UV and R-band scale radii expected from thin disk theory; the flux estimates are smaller by 0.38 dex. The vertical line on the left marks the estimated gravitational radius of the black hole. The mean mass $\langle M \rangle$ is fixed at $0.3 M_\odot$, and all other parameters are marginalized.

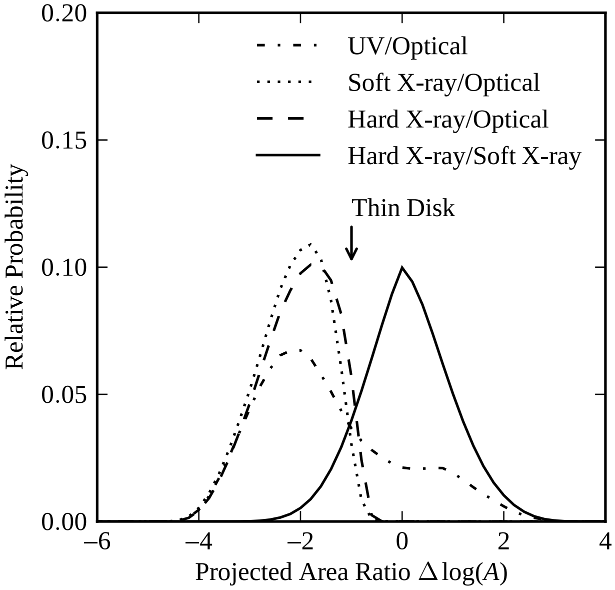

FIG. 6.— Posterior probability distributions for the ratios of projected areas, expressed as logarithmic differences. The arrow denotes the ratio of UV area to optical area predicted by the standard thin disk theory; compare it to the dot-dashed curve. The mean mass $\langle M \rangle$ is fixed at $0.3 M_\odot$, and all other parameters are marginalized. We use a logarithmic prior.

tributions for soft X-ray to optical, hard X-ray to optical, and hard X-ray to soft X-ray. These distributions use a logarithmic prior only, as a linear prior does not make sense for such ratios. We also mark the expected value of the UV to optical ratio for the thin disk case where $\Delta\log A = 8/3 \Delta\log\lambda$. This value is consistent with our probability distribution, which is not surprising given the width of the UV area distribution. Although it is not relevent for the thin disk model, the ratio of hard X-ray area to soft X-ray area is interesting because of the possibility of structure in the X-ray corona. We do not find evidence of a difference in sizes: the distribution peaks just at unity (though it is broad enough that significant differences in the source area at different X-ray energies are not ruled out). This runs a bit counter to the results of Chen et al. (2011), who measure X-ray light curves indicating energy-dependent size differences in Q 2237+0305. More densely-sampled X-ray light curves would be invaluable in addressing this question.

Figure 7 shows the posterior probability distribution for the mean mass of the stars $\langle M \rangle$. Like the source area, this measurement is affected by the resolution limits of our magnification patterns (see Figure 2). To avoid this problem, which would bias our mass results toward smaller mean masses, we use the results of the simulation that is constrained only by the R-band light curve. Like Poindexter & Kochanek (2010b), we partially break the degeneracy between velocity and mean mass by virtue of our dynamic magnification patterns, but as we have mentioned, the small random stellar velocities in the HE 0435 system reduce the power of this method. Indeed, our posterior velocity distribution is indistinguishable from the prior, indicating that we have not strongly broken the degeneracy. Our mean mass probability distribution is consistent with

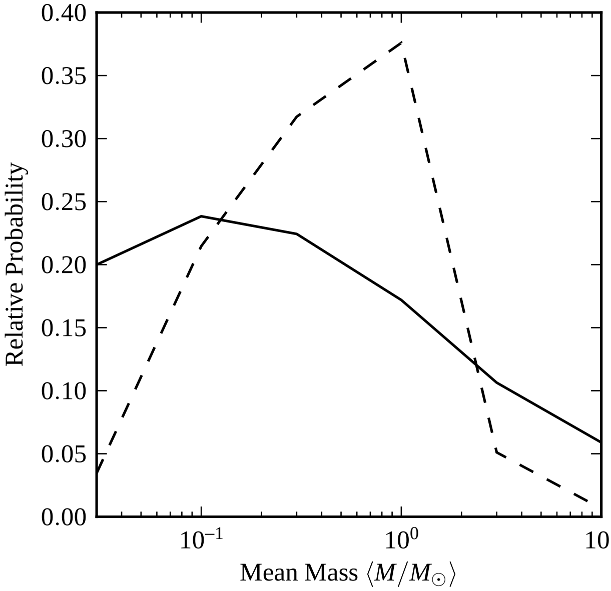

FIG. 7.— Posterior probability distribution for the mean mass $\langle M \rangle$ of the microlens stars. All other parameters are marginalized. This result is taken from the optical-only simulation, to avoid biases arising from the lack of convergence at small X-ray and UV sizes; see text for details. The solid line uses a flat logarithmic prior, while the dashed line uses the result of Poindexter & Kochanek (2010b) as a prior.

other estimates of the mean mass (Poindexter & Kochanek 2010b). Since our posterior probability distribution is independent of that of Poindexter & Kochanek (2010b), we multiply the two distributions together and plot them as a dashed curve in Figure 7. This is equivalent to using their distribution as a prior.

As pointed out by Blackburne & Kochanek (2010), if quasar optical variability is due to changes in the effective area of the accretion disk, there will be a potentially measurable effect on microlensing light curves that depends on ϵ, the power-law slope of the relationship between the source area and the intrinsic quasar luminosity $A(t) \propto L(t)^{\epsilon}$. In the simplest model of a multi-temperature blackbody disk where all the variability is due to changes in disk size, $\epsilon = 1$. With our dynamic magnification patterns, we have the opportunity to test this hypothesis by varying the size of the source according to an estimate of the intrinsic quasar light curve $S(t)$. We repeat one of our microlensing simulations, for simplicity fixing $f_{M/L} = 0.3$ and $\langle M \rangle = 0.3 M_{\odot}$ and restricting ourselves to face-on disks. We adjust the source area at each epoch by a factor equal to a power ϵ of the source flux, keeping the time-averaged source area equal to the fiducial value of the area parameter. We allow ϵ to take values ranging from −1.0 to 2.0 in steps of 0.5. The intrinsic light curve is estimated by averaging the source light curves corresponding to the best-fitting trials from our main optical simulations. The resulting probability distribution for the exponent ϵ allows for the entire simulated range, but favors the lower values. This result argues against the idea that coherent changes in the area of the accretion disk account for quasar variability, and contradicts the preliminary tests of Blackburne & Kochanek (2010), who find qualitative evidence that the area and luminosity of this quasar are positively correlated.

In future microlensing studies using light curves at several UV, optical, and infrared (IR) wavelengths, it would be preferable to parameterize the wavelength dependence of the accretion disk size using a power law, as in Poindexter et al. (2008), rather than using independent size estimates at each wavelength, as we do in this work. The difficulty with this approach is the necessity of modeling all the light curves simultaneously, a task that can quickly outpace our computational (specifically, memory) capacity unless the algorithm is carefully designed. When there are contemporaneous observations at multiple wavelengths, we can save some memory by reusing magnification patterns. Another promising strategy would be to separate the data into a densely-sampled single-wavelength light curve and a second multi-wavelength light curve constructed from relatively sparse light curves at the remaining wavelengths. This would allow the successful trials from the single-wavelength simulation to be used as input for a second, multiple-wavelength simulation where the power-law slope $d\log A/d\log\lambda$ would be allowed to vary. This is functionally equivalent to the approach in the previous paragraph, but with the wavelengths in place of the estimated intrinsic light curve.

Based on eight seasons of *R*-band monitoring data, nine epochs of UV photometry from *HST*, and four epochs of X-ray fluxes in two energy bands from *Chandra*, we have put limits on the projected area and scale radius R_S of the accretion disk of HE 0435 − 1223. Using logarithmic priors, we find in the observed *R* band that the scale radius $\log(R_S/\mathrm{cm})$ is $15.53^{+0.36}_{-0.35}$, or about 46 gravitational radii assuming a black hole mass $M_{\mathrm{BH}} = 5 \times 10^8 M_{\odot}$ (based on a C IV line width measurement; Peng et al. 2006). This large disk size confirms previous results (Morgan et al. 2010; Blackburne et al. 2011; Mosquera et al. 2011), being about 0.4 dex larger than the size predicted by thin disk theory, and 0.8 dex larger than the size estimated from the optical flux. The UV size is more poorly constrained, but we can say that it is most likely smaller than the optical size. In soft (0.4 – 1.3 keV) and hard (1.3 – 8 keV) X-ray energy bands respectively, we can set upper limits of $\log(R_S/\mathrm{cm}) = 14.96$ and 15.07, or 12 and 16 gravitational radii, with at least 90% confidence. We also compute probability distributions for the area ratios between various wavelengths. With a very broad distribution, the UV/optical ratio is consistent with both thin disk theory and with previous estimates of the wavelength slope, and the hard X-ray/soft X-ray area ratio is most consistent with unity. Adopting a range of values for the mean mass $\langle M \rangle$ of the stars in the lens galaxy, we find results consistent with earlier studies, with a most likely range of $0.1 - 1\, M_{\odot}$. Finally, a test of the power-law dependence of the source area on the instantaneous luminosity of the quasar does not support the idea that quasar variability is a simple result of coherent changes in the area of the accretion disk.

This research was supported in part by NSF grant AST-1009756. Support for *HST* programs #11732 and #12324 was provided by NASA through a grant from the Space Telescope Science Institute, which is operated by the Association of Universities for Research in Astronomy, Inc., under NASA contract NAS5-26555. Further support for this work was provided by the National Aeronautics and Space Administration through Chandra Award Number 11121 issued by the Chandra X-ray Observatory Center, which is operated by the Smithsonian Astrophysical Observatory for and on behalf of the National Aeronautics Space Administration under contract NAS8-03060.

REFERENCES

Anguita, T., Schmidt, R. W., Turner, E. L., et al. 2008, A&A, 480, 327

Bate, N. F., Floyd, D. J. E., Webster, R. L., & Wyithe, J. S. B. 2008, MNRAS, 391, 1955

Bertin, E. & Arnouts, S. 1996, A&AS, 117, 393

Blackburne, J. A. & Kochanek, C. S. 2010, ApJ, 718, 1079

Blackburne, J. A., Pooley, D., Rappaport, S., & Schechter, P. L. 2011, ApJ, 729, 34

Blaes, O., Hubeny, I., Agol, E., & Krolik, J. H. 2001, ApJ, 563, 560

Cardelli, J. A., Clayton, G. C., & Mathis, J. S. 1989, ApJ, 345, 245

Chartas, G., Kochanek, C. S., Dai, X., Poindexter, S., & Garmire, G. 2009, ApJ, 693, 174

Chen, B., Dai, X., Kochanek, C. S., et al. 2011, ApJ, 740, L34

Collier, S. 2001, MNRAS, 325, 1527

Congdon, A. B., Keeton, C. R., & Osmer, S. J. 2007, MNRAS, 376, 263

Courbin, F., Chantry, V., Revaz, Y., et al. 2010, A&A, in press (arXiv:1009.1473)

Dai, X., Kochanek, C. S., Chartas, G., et al. 2010, ApJ, 709, 278

DePoy, D. L., Atwood, B., Belville, S. R., et al. 2003, in SPIE Conf. Ser. 4841, Instrument Design and Performance for Optical/Infrared Ground-based Telescopes, ed. M. Iye & A. F. M. Moorwood (Bellingham, WA: SPIE), 827

Dexter, J. & Agol, E. 2011, ApJ, 727, L24

Eigenbrod, A., Courbin, F., Meylan, G., et al. 2008, A&A, 490, 933

Fadely, R. & Keeton, C. R. 2011, AJ, 141, 101

Falco, E. E., Impey, C. D., Kochanek, C. S., et al. 1999, ApJ, 523, 617

Falco, E. E., Kochanek, C. S., Lehár, J., et al. 2001, in ASP Conf. Ser. 237, Gravitational Lensing: Recent Progress and Future Goals, ed. T. G. Brainerd & C. S. Kochanek (San Francisco:ASP), 25
Floyd, D. J. E., Bate, N. F., & Webster, R. L. 2009, MNRAS, 398, 233
Garmire, G. P., Bautz, M. W., Ford, P. G., Nousek, J. A., & Ricker, Jr., G. R. 2003, in SPIE Conf. Ser. 4851, X-Ray and Gamma-Ray Telescopes and Instruments for Astronomy, ed. J. E. Truemper & H. D. Tananbaum (Bellingham, WA: SPIE), 28
Hinshaw, G., Weiland, J. L., Hill, R. S., et al. 2009, ApJS, 180, 225
Hockney, R. W. & Eastwood, J. W. 1981, Computer Simulation Using Particles (New York, NY: McGraw-Hill)
Inada, N., Oguri, M., Falco, E. E., et al. 2008, PASJ, 60, L27
Inada, N., Oguri, M., Keeton, C. R., et al. 2005, PASJ, 57, L7
Keeton, C. R. 2003, ApJ, 582, 17
Kelly, B. C., Bechtold, J., & Siemiginowska, A. 2009, ApJ, 698, 895
Kochanek, C. S. 2004, ApJ, 605, 58
Kochanek, C. S. & Dalal, N. 2004, ApJ, 610, 69
Kochanek, C. S., Morgan, N. D., Falco, E. E., et al. 2006, ApJ, 640, 47
Kozłowski, S., Kochanek, C. S., Udalski, A., et al. 2010, ApJ, 708, 927
MacLeod, C. L., Ivezić, Ž., Kochanek, C. S., et al. 2010, ApJ, 721, 1014
Mao, S., Witt, H. J., & Koopmans, L. V. E. 2001, MNRAS, 323, 301
Morgan, C. W., Kochanek, C. S., Dai, X., Morgan, N. D., & Falco, E. E. 2008, ApJ, 689, 755
Morgan, C. W., Kochanek, C. S., Morgan, N. D., & Falco, E. E. 2010, ApJ, 712, 1129
Morgan, N. D., Kochanek, C. S., Pevunova, O., & Schechter, P. L. 2005, AJ, 129, 2531
Mortonson, M. J., Schechter, P. L., & Wambsganss, J. 2005, ApJ, 628, 594
Mosquera, A. M. & Kochanek, C. S. 2011, ApJ, 738, 96
Mosquera, A. M., Muñoz, J. A., Mediavilla, E., & Kochanek, C. S. 2011, ApJ, 728, 145
Novikov, I. D., & Thorne, K. S. 1973, in Black Holes (Les Astres Occlus), ed. C. Dewitt & B. S. Dewitt (New York, NY: Gordon & Breach), 343
Peng, C. Y., Impey, C. D., Rix, H.-W., et al. 2006, ApJ, 649, 616
Poindexter, S. & Kochanek, C. S. 2010a, ApJ, 712, 668
Poindexter, S. & Kochanek, C. S. 2010b, ApJ, 712, 658
Poindexter, S., Morgan, N., & Kochanek, C. S. 2008, ApJ, 673, 34
Pooley, D., Blackburne, J. A., Rappaport, S., & Schechter, P. L. 2007, ApJ, 661, 19
Pooley, D., Rappaport, S., Blackburne, J. A., Schechter, P. L., & Wambsganss, J. 2011, ApJ, submitted (arXiv:1108.2725)
Reynolds, C. S. & Nowak, M. A. 2003, Phys. Rep., 377, 389
Rusin, D., Keeton, C. R., & Winn, J. N. 2005, ApJ, 627, L93
Rusin, D. & Ma, C.-P. 2001, ApJ, 549, L33
Schechter, P. L., Mateo, M., & Saha, A. 1993, PASP, 105, 1342
Schlegel, D. J., Finkbeiner, D. P., & Davis, M. 1998, ApJ, 500, 525
Shakura, N. I. & Sunyaev, R. A. 1973, A&A, 24, 337
Treu, T., Koopmans, L. V., Bolton, A. S., Burles, S., & Moustakas, L. A. 2006, ApJ, 640, 662
Weisskopf, M. C., Brinkman, B., Canizares, C., et al. 2002, PASP, 114, 1
Winn, J. N., Rusin, D., & Kochanek, C. S. 2004, Nature, 427, 613
Wisotzki, L., Schechter, P. L., Bradt, H. V., Heinmüller, J., & Reimers, D. 2002, A&A, 395, 17
Wyithe, J. S. B., Webster, R. L., & Turner, E. L. 2000, MNRAS, 315, 51